PAPER

Check for updates

Influence of N-protonation on electronic properties of acridine derivatives by quantum crystallography†

Sylwia Pawlędzio, [ID] *ab Marcin Ziemniak, [ID] b Damian Trzybiński, [ID] b
Mihails Arhangelskis, [ID] b Anna Makal b and Krzysztof Woźniak [ID] *b

Applications of 9-aminoacridine (**9aa**) and its derivatives span fields such as chemistry, biology, and medicine, including anticancer and antimicrobial activities. Protonation of such molecules can alter their bioavailability as weakly basic drugs like aminoacridines exhibit reduced solubility at high pH levels potentially limiting their effectiveness in patients with elevated gastric pH. In this study, we analyse the influence of protonation on the electronic characteristics of the molecular organic crystals of 9-aminoacridine. The application of quantum crystallography, including aspherical atom refinement, has enriched the depiction of electron density in the studied systems and non-covalent interactions, providing more details than previous studies. Our experimental results, combined with a topological analysis of the electron density and its Laplacian, provided detailed descriptions of how protonation changes the electron density distribution around the amine group and water molecule, concurrently decreasing the electron density at bond critical points of N/O−H bonds. Protonation also alters the molecular architecture of the systems under investigation. This is reflected in different proportions of the N···H and O···H intermolecular contacts for the neutral and protonated forms. Periodic DFT calculations of the cohesive energies of the crystal lattice, as well as computed interaction energies between molecules in the crystal, confirm that protonation stabilises the crystal structure due to a positive synergy between strong halogen and hydrogen bonds. Our findings highlight the potential of quantum crystallography in predicting crystal structure properties and point to its possible applications in developing new formulations for poorly soluble drugs.

1. Introduction

Acridines are a class of heterocyclic compounds composed of a tricyclic aromatic system being a derivative of anthracene with one central CH group replaced by a nitrogen atom. Acridine-based derivatives have found several applications in the fields of chemistry, biology, and medicine such as fluorescent dyes,[1] drugs[2] and catalysts in organic synthesis.[3,4] Despite being generally toxic and carcinogenic in mammals, 9-aminoacridine (**9aa**) has found several applications in medicinal chemistry, since it provides a scaffold for synthesizing several molecules, which display promising anticancer and antimicrobial activities.[3] In living cells, aminoacridines mainly act by DNA intercalation[5,6] and inhibition of topoisomerase II,[7] disrupting DNA replication and, thereby, cell division making them useful antimalarial[8] and anticancer drugs.[9] Since **9aa** derivatives often display specificity against particular types of cancer cells their mechanisms of action are not merely limited to DNA damage and it is believed that it also includes the disruption of several signalling pathways including PI3K/AKT/mTOR, p53 and NF-kappaB[10] as well as induction of apoptosis.[11] Interestingly, the antimalarial activity of acridines is also a complex phenomenon involving inhibition of topoisomerase II, mitochondrial proteins and formation of hemozoin, a by-product of haemo-globin decomposition crucial for heme detoxification in *Plasmodium*.[12,13] Due to their potential efficacy against drug-resistant strains of *Plasmodium* sp., which are becoming more prevalent than in previous years, interest in acridines and their derivatives has also increased.[8,13]

The structural chemistry of acridines is quite well described.[14–16] Most of the reported structures of **9aa** are multi-component systems containing other chemical entities in their crystal lattices, often inorganic anions or solvent molecules.[17–21] Acridine moieties are usually protonated, and intricate patterns of hydrogen bonding stabilise their crystal structures. It is

aNeutron Scattering Division, Oak Ridge National Laboratory, Oak Ridge, TN 37831, USA. E-mail: pawledzios@ornl.gov

bDepartment of Chemistry, Biological and Chemical Research Centre, University of Warsaw, Żwirki i Wigury 101, 02-093, Warszawa, Poland. E-mail: kwozniak@chem. uw.edu.pl

known that **9aa** can form different crystal structures depending on the type of ions and/or solvent molecule(s) present in the crystals. Monohydrates of **9aa** halides form π-stacked columns along the *Y*(*b*)-direction which are linked *via* a N–H⋯O hydrogen bond between the endocyclic N-atom of the acridinium ring and a water molecule to produce a complex 3D architecture.[20] These structures usually contain an $R^2_2(8)$ structural motif consisting of two molecules (**9aa** and halogen anions, or a water moiety and a halogen anion) related by a twofold rotation axis and held together by eight hydrogen bonds. Bis-hydrated **9aa** halides display similar structural features. However, their complexity is even higher since their crystals contain several different supramolecular rings.[20] The structure of the hemihydrate of **9aa** is also known and is composed of supramolecular tetramers of **9aa** molecules connected *via* water-bridged hydrogen bonds, and no stacking interactions are present in the crystal.

It is well known that due to changes in its bioavailability upon protonation, the protonated form of a drug may have different pharmaceutical potency than the neutral form.[22] In many cases, only a drug's non-protonated form can readily penetrate cell membranes when active transport is not involved.[23] On the other hand, many weakly basic drugs, including aminoacridines, have reduced solubility at higher pH. This may become a significant issue in patients with achlorhydria or other conditions leading to high gastric pH, which could reduce the bioavailability of these drugs.[24,25] The reduced absorption of weakly basic drugs under high gastric pH can be mitigated by several strategies including pre-treatment with organic acids,[26] or the development of formulations containing either acidic salts or solid dosage formulations, in which an acid acts as pH modifying factor enhancing the bioavailability in the stomach.[24] The last strategy is promising due to its simplicity and is under clinical investigation.[27]

The dynamic development of technology, X-ray diffraction equipment and dedicated computer software have made X-ray structural analysis of single crystals the most important method for determining the structure of chemical compounds. Thousands of structures are deposited annually in the CSD (Cambridge Structural Database). Determining the structure of a molecule with pharmaceutical properties (API, Active Pharmaceutical Ingredient) is linked to studies of its electronic properties and the intermolecular interactions. Aspherical atom refinement is a quantum crystallographic method used to refine crystal structures with a more accurate description of the electron density (ED) distribution than other methods.[28–31] In traditional refinement methods such as the Independent Atom Model (IAM), atomic EDs are modelled as spherical, which is a crude approximation of the real distribution of the ED in the crystalline solid state. Aspherical atom refinement considers the non-spherical nature of the electron density distribution around atoms providing more accurate structural parameters, displacement parameters, and hydrogen-bond lengths compared to traditional refinement methods.[32,33] Aspherical atom refinement can be performed using various quantum crystallographic methods, including Hirshfeld atom refinement (HAR).[34,35] HAR uses aspherical atomic scattering factors obtained from the quantum-mechanical calculation of electron density (usually using DFT methods) to refine X-ray crystal structures[36,37] and is the most advanced method of refining X-ray crystal structures, providing structural parameters for hydrogen atoms including both the H-atom positions and their anisotropic displacement parameters.[38,39] Another advantage of HAR is the capability to include the crystal environment during the refinement, which can improve its quality when compared to IAM or MM/TAAM methods based on the pseudo-atom approach.[34] Additionally, HAR seems to be effective even in the case of routine diffraction data.[40]

Despite that accurate and precise structural information may be obtained from HAR, there are only few studies dedicated to topics such as patterns of hydrogen bonds in the crystal, or the presence of structural clashes between the neighbouring atoms. Such information may allow to design of new drug formulations with improved bioavailability,[33] since materials/drug properties are related to the electronic structure and accuracy of its determination. The previously mentioned papers focus on structural and biochemical studies on compounds with potential pharmaceutical properties including anticancer[41] and antiviral activities.[42] In one study dedicated to protein–ligand interactions, it was found that ED polarization of the ligand molecule in the protein binding pocket could be used to predict the electrostatic features of the binding itself. However, these experimental results are difficult to interpret.[43] In other studies, application of HAR, or electron-density analysis, was rather limited since it was not the focus of the research. The protonation and its influence on hydrogen bonding in crystals of urea derivatives and their co-crystals was the subject of one study which utilised HAR among other methods.[44]

In this study, we decided to apply computational quantum chemistry tools, including periodic DFT calculations and topological analysis of electron density derived from molecular wavefunctions, to HAR to achieve better understanding the influence of protonation on electronic properties of 9-aminoacridine in the crystalline solid state. We investigated the
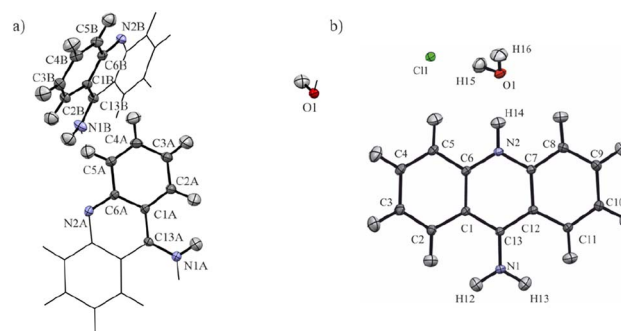

Fig. 1 The asymmetric unit of (a) 9-aminoacridine hemihydrate (**9aa***H_2O) and (b) 9-aminoacridine hydrochloride monohydrate (**9aa***HCl) with the labelling scheme. Atomic displacement ellipsoids are shown at a 50% probability level. The non-asymmetric unit of 9-aminoacridine hemihydrate is represented by sticks for the sake of clarity.

influence of protonation on the intermolecular interactions and ED topological properties on the 9-aminoacridine moieties for 9-aminoacridine hemihydrate (**9aa*H₂O**) and 9-aminoacridine hydrochloride monohydrate (**9aa*HCl**) (Fig. 1).

Protonation also modifies the intermolecular interactions by changing the proportion of the N···H and O···H contacts, and the number of C···H and H···H interactions. Theoretical calculations reveal that protonation stabilizes the crystal structure due to the presence of strong halogen and hydrogen bonds which compensates for the destabilizing effect of the interactions between two 9-aminoacridine moieties. Finally, we investigate the effect of **9aa** protonation on its binding to selected DNA and protein molecules.

2. Experimental

2.1. Materials and crystallization procedures

The **9aa*H₂O** and **9aa*HCl** were purchased from Sigma Aldrich and used without further purification. Small amount of both substances were dissolved in a mixture of ethanol and water (1 : 1; v : v) and then heated for several minutes. In the next step, the solutions were left to slowly evaporate at room temperature until the appearance of crystals. Typical representatives of single crystals from both samples are shown in Fig. 2.

2.2. Data collection

Data was collected for both crystals at different resolutions. For the **9aa*H₂O** dataset, we were only able to collect low-resolution data (Table 1) due to the weakly diffracting sample. X-ray data were taken at 100(2) K using an Agilent Technologies SuperNova Dual Source diffractometer (CuKα radiation, $\lambda = 1.54184$ Å). For the **9aa*HCl** dataset, we have collected high-resolution X-ray diffraction data at 100(2) K on a Bruker AXS Kappa APEX II Ultra diffractometer equipped with a rotating anode (Mo Kα radiation, $\lambda = 0.71073$ Å). The data set was integrated with *CrysAlis* (CrysAlisPRO, Oxford Diffraction/Agilent Technologies UK Ltd, Yarnton, England) and *APEX2* (ref. 45) packages for the **9aa*H₂O** and **9aa*HCl** datasets respectively. Data sets were also corrected for Lorentz and polarization effects.[46] The absorption correction from crystal shape was applied to the **9aa*H₂O** and **9aa*HCl** datasets respectively. Reflections were merged with *SORTAV*.[47] Experimental details and refinement parameters for both compounds are summarized in Table 1.
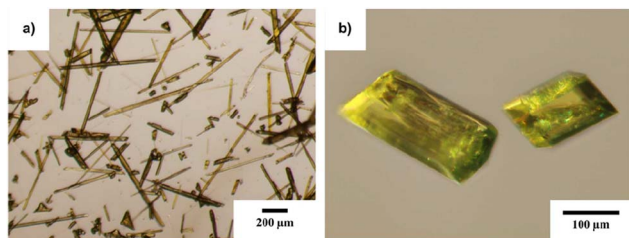

Fig. 2 Overall view on the single crystals of 9-aminoacridine hemihydrate (a) and 9-aminoacridine hydrochloride monohydrate (b) grown from ethanol : water mixture (1 : 1; v : v).

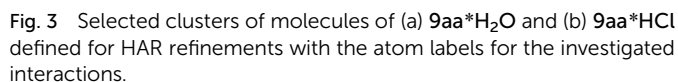**Table 1** Experimental details of investigated compounds

	9aa*H₂O	9aa*HCl
Crystal system	Tetragonal	Triclinic
Space group	$I4_1/acd$	$P\bar{1}$
Empirical formula	$C_{26}H_{22}N_4O_1$	$C_{13}H_{13}ClN_2O$
Formula weight	406.48	248.70
a/Å	24.310(2)	7.7880(5)
b/Å	24.310(2)	8.7699(5)
c/Å	14.016(2)	9.7291(6)
α/°	90	111.057(2)
β/°	90	96.558(2)
γ/°	90	104.436(2)
Volume/Å³	8283.6(17)	585.08(6)
Z	16	2
μ/mm⁻¹	0.647	0.310
T_{max}	0.927	0.981
T_{min}	0.888	0.958
ρ_{calc}/mm³	1.304	1.412
$F(000)$	3424	260
Crystal size/mm³	0.08 × 0.09 × 0.14	0.18 × 0.20 × 0.31
R_{int}	0.0384	0.0275
R_{sigma}	0.0383	0.0259
hkl index ranges	27 : −29	16 : −16
	26 : −29	17 : −18
	10 : −16	20 : 0
Reflections collected	7758	11 578
2θ range for data collection	3.36 to 52.14	4.6 to 97.52
Temperature/K	100(2)	100(2)
X-ray wavelength/Å	1.54184	0.71073
Independent reflections	2017	11 578

2.3. Structure solution and refinement

The structural determination procedure for both crystal structures was carried out using *SHELX* package.[48–50] The structures were solved with direct methods,[48] and then successive least-squares refinements were performed based on full-matrix least-squares on F^2 using *SHELXL*[49] with the graphical interface of *Olex2* software.[51] All H atoms were positioned geometrically with the C–H bond length equal to 0.93 Å for the aromatic hydrogen atoms, 0.85 Å for the hydroxyl hydrogen atom and 0.88 Å for the amine hydrogen atoms and constrained to ride on their parent atoms with $U_{iso}(H) = xU_{eq}(C)$, where $x = 1.2$ for the aromatic and amine H atoms and $x = 1.5$ for the hydroxyl H atom.

Aspherical structural refinements (HAR approach) were carried out using *Discamb*,[52] our in-house program, connected to the *Olex.refine* engine.[53] The calculations of the molecular wavefunction were performed with the ORCA 5.0 package[54,55] at the B3LYP[56]/cc-pVDZ[57] levels of theory. The SCF calculations were performed for cluster of molecules, defined in such a way as to enable investigation of the intermolecular interactions present in the crystal structures as presented in Fig. 3. Also a cluster of charges and dipoles was applied during SCF calculations in order to simulate the crystal environment[58,59] of all the neighbouring molecules, which have any atom within a radius of 16 Å from the central molecule. During refinement, all atomic positions were refined without any constraints or restraints applied. ADPs were computed and refined only for C, N and O,

Fig. 3 Selected clusters of molecules of (a) **9aa*H₂O** and (b) **9aa*HCl** defined for HAR refinements with the atom labels for the investigated interactions.

while H atoms were estimated using *SHADE3* server[60] and fixed during the refinements.

Selected final statistics for all refinements are given in Table 1. More information can be found in the .cif files (deposition numbers 2270291–2270294†).

2.4. Topological analysis

The analysis of the electron density distribution obtained during HAR refinement was performed according to the Bader's Quantum Theory of Atoms in Molecules (QTAIM) formalism[61] in *AIMAll* software.[62]

2.5. Theoretical calculations

Geometry optimization under periodic conditions was carried out with *Crystal09* (ref. 63) for the **9aa*H₂O** dataset and *Crystal17* (ref. 64) for the **9aa*HCl** dataset, respectively, at the B3LYP[56]/cc-pVTZ[65] level of theory with an employed Grimme dispersion[66,67] and BSSE corrections.[68] In both cases, we have used the lattice parameters and experimental geometry obtained from X-ray diffraction experiments and run optimization of the atomic positions only. Consequently, cohesive crystal lattice and dimer interaction energies based on those optimized geometries were calculated according to the case described for molecular crystals available at **https://www.crystal.unito.it**/website. Hirshfeld surface analysis was done with *CrystalExplorer17* (ref. 69) at the B3LYP/6-31G(d,p) level of theory for the geometry obtained from theoretical periodic calculations. Electrostatic potential (ESP)[70] was computed using *Multiwfn*3.8 (ref. 71) program using a molecular wavefunction from the HAR refinement.
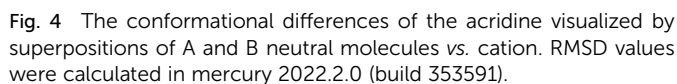
2.6. Macromolecular studies

Selected structures were downloaded from PDB database. To each structure hydrogen atoms were added, and local geometry optimisation was performed (heavy atoms in the protein or DNA molecules were fixed) using *Chimera 1.17* program and surface analyses for bound ligands were calculated in *CrystalExplorer17*. For DFT calculations selected fragments of structures were tailored in *ChimeraX*[72] program and all computations were performed in *ORCA* 5.0 package using ChimeraX and the *SEQ-CROW*[73] bundle as a graphical interface. Molecular wavefunction were calculated at the ωB97X-D3/def2-SVP[74,75] level of theory using an implicit SMD solvent model.[76] All ED functions were calculated in *Multiwfn* and visualised in *ChimeraX*.

3. Results and discussion

3.1. Crystal structures

The first deposition of crystal structures determined from single crystal XRD measurement at room temperature for both, the **9aa*H₂O** and **9aa*HCl**, have been done by Chaudhuri in 1983 (ref. 77) and by Talacki in 1973,[78] respectively. Here, we have reinvestigated the crystal structures of both forms at 100 K. Similarly, to the previously reported work, we have found that **9aa*H₂O** crystallized in the tetragonal, body centred $I4_1/acd$ space group with two halves of the **9aa** molecules (hereafter called A and B molecules) and half of a water molecule in the asymmetric part of the unit cell (Fig. 1).

On the other hand, **9aa*HCl** crystallized in the triclinic $P\bar{1}$ space group with one of the acridine and chloride ions and one water molecule in asymmetric part (Fig. 1). In both investigated systems, the anthracene ring is planar, with the amine group directed almost in its plane. Protonation virtually does not change acridine's geometry (Fig. 4), and the main differences between the acridine moiety for the neutral *vs.* protonated forms come from the slightly different orientations of the amine group. In the case of the **9aa*H₂O**, the dihedral angle between the planes defined by the anthracene ring and amine group is around 0.32° and 8.69° for A and B molecules, respectively. For the acridine cation this angle is equal to 8.35°, however, orientation of the amine group is different than those observed for the neutral form B molecule. Numerical values of the bond lengths can be found in the ESI (Tables S3 and S4†) or in the .cif files.

3.2. Comparison of different models of electron density

The details of the spherical and aspherical refinements are presented in Table 2. The advantage of using aspherical approaches over the IAM model[79] is evident in both cases and supported by general refinement agreement indicators. However, applying aspherical refinement did not improve residual density values for the **9aa*H₂O**, contrary to the refinements of the **9aa*HCl**. Differences in data resolution might cause this, and in the case of **9aa*H₂O** for which we collected only the low-angle data, the residual density is mainly located on the outermost parts of benzene rings. This residual electron density may suggest some structural disorder which is not resolvable here (Fig. S1†).

For the **9aa*HCl**, the differences between residual density after IAM and HAR are more noticeable. According to the theoretical calculations, the residual density after aspherical

Fig. 4 The conformational differences of the acridine visualized by superpositions of A and B neutral molecules *vs.* cation. RMSD values were calculated in mercury 2022.2.0 (build 353591).

Table 2 Spherical and aspherical refinements details

	9aa*H$_2$O		9aa*HCl	
	IAM	HAR	IAM	HAR
$R(F^2)$	5.48%	4.30%	2.80%	1.86%
wR^2	12.80%	9.10%	7.88%	4.26%
Data	2017	2017	11 578	11 578
Restraints	0	0	0	0
Parameters	153	177	206	193
GooF	1.041	0.911	1.064	1.178
Largest diff. peak/hole (e Å^{-3})	0.15/−0.29	0.21/−0.26	0.59/−0.33	0.36/−0.29

refinement is mainly located on chloride anion and in the vicinity of oxygen lone pairs (Fig. S2†). Also, the X–H bond lengths are significantly improved after aspherical refinement with the bond lengths as those obtained by neutron diffraction studies (Tables S1 and S2†).

3.3. Electron density distribution

The values of the electron density (ED) and its Laplacian at the selected BCPs for the **9aa*H$_2$O** and **9aa*HCl** are shown in Fig. 5 and Table 3. The bonding situation around the amino groups, water molecules and nitrogen atoms is different in neutral and protonated forms of **9aa**, and we compare differences between these two systems. Firstly, there are no changes in the corresponding bond lengths due to the protonation effect within a particular type of refinement (Tables 3, S1 and S2†).

Fig. 5 and Table 3 both show that the protonation of the nitrogen atom (N2A/B) do not have noticeable impact on the

Fig. 5 Molecular graphs after HAR with the electron density (upper) and its Laplacian (lower and bold) values at BCPs for the: (a) **9aa*H$_2$O** and (b) **9aa*HCl** forms. BCPs are shown as small green spheres.

values of the ED at the BCP for N2A/B–C6A/B vs. N2–C6 bonds. The difference in electron density observed at this BCP after protonation is around 0.11 e Å^{-3} with very small differences visible in the Laplacian values (ca. 4 e Å^{-5}). Further examination of the C1–C6 and C1–C13 bonds (see Table 3 and Fig. 5 for details) shows no significant changes in the values of the ED and its Laplacian after protonation.

When looking at the BCP values for the anthracene rings (Tables S3 and S4†), we can immediately see that the delocalization of the electron density in this region of the moiety is not observed. Instead, increases and decreases of charge distribution with a simultaneous slight change of the C–C bond lengths are observed. This pattern is preserved in both **9aa** forms, despite the different molecular architectures of these crystal, and thus, indicating that even disparate patterns of intermolecular interactions have the same impact on ED distribution within the polycyclic system (Fig. S3†). Notably, the absence of pure delocalization of the electron density followed by a specific change of C–C bond lengths structures agrees with the previously published results for structures containing **9aa** or its derivatives.

Furthermore, it appears that the primary differences in electron density distributions between **9aa*H$_2$O** and **9aa*HCl** are in the amine group region and stemmed from the presence of the N–H···Cl interaction. These interactions cause an increase in the ED and its Laplacian at the BCP for the C13–N1 bond and decrease for the N1–H12/13 bond, when comparing the neutral A molecule and protonated forms (as shown in Fig. 5 and Table 3). This observation is slightly different when looking at the neutral B molecule since for both bonds the increase of ED at BCP is observed. For the water molecule, when examining the values at the BCP after protonation, a decrease in the ED and its Laplacian is observed only for one O–H bond, namely O1–H15 (Fig. 5 and Table 3). This may suggest that HAR is sensitive for this type of interactions, particularly because one would expect a non-equivalent behaviour of these two bonds due to different interactions with other atoms in their close vicinity (Fig. S4†).

The integration of the electron density over atomic basins also provided the charge and basin volumes of atoms (Table 4). In principle, protonation should change the curvature of regions bounded by zero-flux surfaces, and thus affects atomic charges basin volumes. As it is summarised in Table 4, the protonation of the N2A atom resulted in a change of its atomic
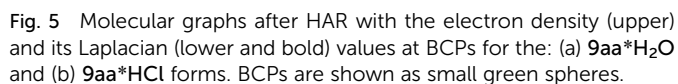
Table 3 Selected QTAIM parameters at BCPs for **9aa*H₂O** and **9aa*HCl**

9aa*H₂O

Bond	d (Å)	ρ_{BCP} (e Å⁻³)	$\nabla^2\rho_{BCP}$ (e Å⁻⁵)	ε
N1A–H12A	1.01	2.27	−39.43	0.04
N1A–C13A	1.34	2.21	−23.75	0.05
C1A–C13A	1.42	1.98	−17.00	0.17
C1A–C6A	1.42	1.98	−16.68	0.18
C6A–N2A	1.35	2.25	−26.95	0.09
N1B–H12B	1.03	2.12	−35.82	0.04
N1B–C13B	1.34	2.25	−23.38	0.06
C1B–C13B	1.43	1.96	−16.77	0.17
C1B–C6B	1.42	1.99	−16.79	0.18
C6B–N2B	1.36	2.23	−26.17	0.10
O1–H15	0.96	2.31	−61.66	0.20

9aa*HCl

Bond	d (Å)	ρ_{BCP} (e Å⁻³)	$\nabla^2\rho_{BCP}$ (e Å⁻⁵)	ε
N1–H13	1.02	2.16	−37.30	0.03
N1–H12	1.02	2.16	−37.11	0.03
N1–C13	1.32	2.32	−24.41	0.07
C1–C13	1.44	1.94	−16.59	0.15
C1–C6	1.41	2.03	−17.63	0.20
C6–N2	1.36	2.14	−22.83	0.07
N2–H14	1.05	2.02	−34.09	0.03
O1–H15	0.97	2.25	−55.10	0.02
O1–H16	0.95	2.41	−65.82	0.02

Table 4 Atomic charges Q_{AIM} and atomic basin volumes V_{AIM} for investigated compounds obtained from integration of the electron density over atomic basins

9aa*H₂O			**9aa*HCl**		
Atom	Q_{AIM} (e)	V_{AIM} (Å³)	Atom	Q_{AIM} (e)	V_{AIM} (Å³)
N1A	−1.35	16.76	N1	−1.36	16.51
N2A	−1.23	15.56	N2	−1.33	13.98
H12A	0.51	2.53	H12	0.52	2.62
C13A	0.54	8.53	H13	0.52	2.67
N1B	−1.36	16.61	C13	0.62	8.30
N2B	−1.22	17.41	H14	0.57	2.16
H12B	0.50	3.71	O1	−1.34	19.71
C13B	0.56	8.50	H15	0.64	2.17
O1	−1.32	19.79	H16	0.65	2.06
H15	0.66	1.81	Cl1	−0.85	39.40

charge and basin volume by −0.10 e and 2.58 Å³, respectively. However, when looking at other atoms, the effect of protonation appears to be small.

3.4. Intermolecular interactions

Fig. 6 shows fingerprint plots and percentage contributions to the Hirshfeld surface of each type of intermolecular contact. One of the most prominent features in all the presented fingerprint plots is the presence of sharp "spikes" in their bottom regions. They are associated with the appearance of some strong O–H⋯Cl, N–H⋯O and O–H⋯N hydrogen bonds in the crystal structures. The positions and shapes of the spikes before and after protonation are different for individual moieties, indicating that protonation and presence of the chloride anion affect hydrogen bond patterns, which is consistent with previously reported results.[80]

In the case of the acridine moiety, the introduction of an H atom has a significant effect on the contribution of N⋯H and O⋯H contacts. Due to the different molecular arrangement of the **9aa** moiety in both forms, **9aa** participates in fewer N⋯H contacts after protonation (12.4/11.6% *vs.* 3.3% for the **9aa*H₂O** mol A/B and **9aa*HCl**, respectively, Fig. 6). This difference is also reflected in the two-dimensional fingerprint
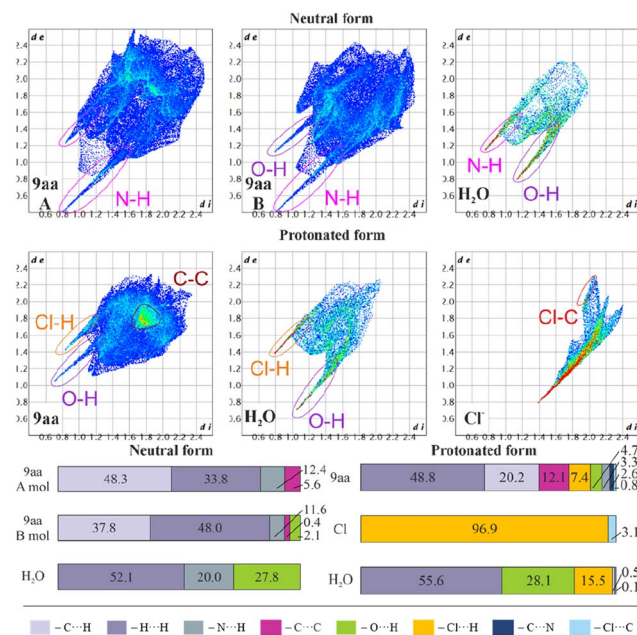
Fig. 6 Hirshfeld surfaces: two-dimensional fingerprint plots (upper) and percentage contributions to the Hirshfeld surface area of each type of intermolecular contact (lower) for **9aa*H₂O** and **9aa*HCl**.

plots, where the sharp spike associated with N⋯H contacts disappears in the **9aa*HCl**. On the contrary, the contribution of the O⋯H contacts almost doubled with the protonation (2.1% *vs.* 4.7% for the **9aa*H₂O** (mol B) and **9aa*HCl**, respectively, as shown in Fig. 6).

Another visible effect of protonation for the **9aa** moiety is a reduced contribution of the C⋯H contacts from 48.3/37.8% to 20.2% (Fig. 6) in favour of an increased contribution of the H⋯H contacts (33.8/48.0% *vs.* 48.8% for the **9aa*H₂O** (mol A/B) and **9aa*HCl**, respectively, Fig. 6). Additionally, the area of the two-dimensional fingerprint plot associated with the C⋯C contacts looks different after protonation (Fig. 6). The density of the plot in this area is substantially higher which is evidence of larger fraction of surface points participating in C⋯C contacts (π-stacking) in the protonated form than in the neutral one.
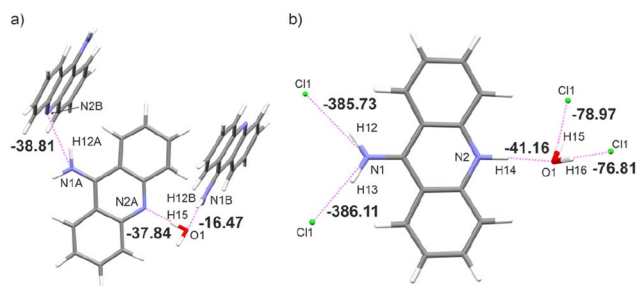
Fig. 7 Dimer energies in kJ mol^{-1} of interacting molecules for: (a) 9aa*H$_2$O and (b) 9aa*H$_2$O.

Naturally, for the **9aa*HCl**, contributions of the Cl···H, Cl···C, and C···N contacts are observed, mostly due to the presence of a chloride anion interacting with the –NH$_2$ group.

The influence of protonation on the acridine molecule is also visible in the contribution of interatomic contacts for water molecules, which is reflected in the increased contribution of the H···H contacts (52.1% *vs.* 55.6% for the **9aa*H$_2$O** and **9aa*HCl**, respectively, Fig. 6). The change in the contribution of the H···H contacts is small when looking at merely its numerical values, but a closer examination of two-dimensional fingerprint plots suggests a more densely packed arrangement of water molecules before protonation. On the other hand, protonation also results in slightly closer-packed planes of the **9aa** moieties in crystal structures (Fig. S5†), which is also reflected in the two-dimensional fingerprint plots (the sum of the d_e and d_i for the protonated form is smaller than for the neutral

form, Fig. 6). In summary, the overall crystal packing seems to be less crowded for **9aa*HCl**, than for **9aa*H$_2$O** (Fig. S5†).

The total crystal lattice cohesive energies are −116.71 and −241.87 kJ mol^{-1} for the **9aa*H$_2$O** and **9aa*HCl**, respectively. The energy decreases significantly after protonation, indicating its stabilising character. The tighter packing of the layers defined by the acridine ions for the **9aa*HCl** form results in the formation of higher number of the weak intermolecular interactions between **9aa** moieties than for the **9aa*H$_2$O** form, which is illustrated with more H···H contacts than C···H or N···H ones after protonation (as shown in Fig. 6).

This generally contributes to the overall destabilisation of the crystal lattice, with dimers defined between **9aa** cations having energies of 166.76 kJ mol^{-1} and 145.69 kJ mol^{-1} (Fig. S6†). In this case, the most stabilising interactions in the crystal lattice are strong N–H···Cl, N–H···O and O–H···Cl hydrogen bonds (Fig. 7b). The chloride anion appears to act as a "molecular glue" that holds the entire crystal lattice together, with energy values of approximately −386.0 kJ mol^{-1} and −78.0 kJ mol^{-1}, mostly due to electrostatically-assisted N–H··· Cl and O–H···Cl contacts, respectively. The interaction energy between **9aa** cation and a water molecule has a typical value of −41.16 kJ mol^{-1}, mostly associated with the strong N–H···O hydrogen bond. Furthermore, the less crowded molecular arrangement observed in **9aa*HCl** may reduce the number of repulsive interactions in the crystal lattice, increasing its stabilising character. In contrast, the crystal structure of the **9aa*H$_2$O** is mainly stabilised *via* weak C–H···π contacts observed between the **9aa** molecules.

Table 5 Topological properties at the critical points and source contributions to the critical point of hydrogen bonds for the **9aa*H$_2$O** and **9aa*HCl**

9aa*H$_2$O

Hydrogen bonds	D···A (Å)	H···A (Å)	DHA (°)	ρ_{BCP} (e Å^{-3})	$\nabla^2\rho_{BCP}$ (e Å^{-5})	H_r (Haa$_0^{-3}$)
O1–H15···N2A	2.869	1.909	174.8	0.22	2.20	0.00
N1B–H12B···O1	2.828	1.895	148.7	0.21	2.35	0.00
N1A–H12A···N2B	3.043	2.064	163.9	0.16	1.52	0.00

Hydrogen bonds	S(D) (%)	S(H) (%)	S(A) (%)	S(D + H + A) (%)
O1–H15···N2A	61.04	−22.01	5.58	44.61
N1B–H12B···O1	54.54	−24.71	44.80	74.63
N1A–H12A···N2B	49.80	−34.91	−10.83	4.06

9aa*HCl

Hydrogen bonds	D···A (Å)	H···A (Å)	DHA (°)	ρ_{BCP} (e Å^{-3})	$\nabla^2\rho_{BCP}$ (e Å^{-5})	H_r (Haa$_0^{-3}$)
O1–H16···Cl1	3.152	2.212	176.6	0.17	1.63	0.00
O1–H15···Cl1	3.159	2.192	169.12	0.16	1.60	0.00
N1–H13···Cl1	3.22	2.264	155.43	0.16	1.41	0.00
N1–H12···Cl1	3.217	2.249	157.35	0.16	1.44	0.00
N2–H14···O1	2.765	1.718	174.96	0.30	3.41	0.00

Hydrogen bonds	S(D) (%)	S(H) (%)	S(A) (%)	S(D + H + A) (%)
O1–H16···Cl1	64.41	−29.69	51.51	86.24
O1–H15···Cl1	70.36	−35.68	51.77	86.45
N1–H13···Cl1	43.95	−30.17	48.82	62.60
N1–H12···Cl1	43.48	−28.96	49.08	63.60
N2–H14···O1	27.13	−3.15	38.19	62.17

The values of such interaction energies range from -6.48 kJ mol^{-1} to -16.67 kJ mol^{-1} (Fig. S7†) and the largest interaction energies were found between the two **9aa** molecules and **9aa A** and water moiety, mostly due to the N–H⋯N and the O–H⋯N H-bonds, respectively (Fig. 7a). Nonetheless, these interactions are not the dominant contributors to the Hirshfeld surface, and the water molecule interacts with two acridine molecules with different strengths (Fig. 7a).

To achieve a more elaborate description of hydrogen bonding in the studied systems, we have also examined topological properties of the electron density at BCP and the source contribution[81] to the BCP (Table 5) for all hydrogen bonds. The source function,[81] which is highly sensitive to electron density perturbations, can reveal subtle changes in local electron density, and thus be a valuable tool for characterising bonding features of hydrogen bonds.[82,83]

The overview of the topological properties of hydrogen bonds is presented in Table 5, and all of them were identified as closed-shell interactions (small value of the electron density and small and positive value of the Laplacian of electron density) of relatively medium-strength (small value of the total energy density, H_t).[84,85] For the **9aa*H$_2$O**, the O1–H15⋯N2A hydrogen bond is the strongest one among the all-existing H-bonds in the crystal structure in terms of the H⋯A distance and topological properties. Similarly, in the case of the **9aa*HCl**, the strongest hydrogen bond is the N2–H14⋯O1 interaction. Noteworthy, protonation does not change either the strength or the character of the hydrogen bonds.

The percentage contribution of the hydrogen atoms to the electron density at the bond critical points for the studied hydrogen bonds is negative in all cases (Table 5). This indicates the electrostatic character of these bonds, and is also typical for the polarization-assisted hydrogen bonds.[81] In almost all cases, the source contribution from the atom triad $S(D + H + A)\%$ has its value above 50% (the exceptions are O1–H15⋯N2A and N1A–H12A⋯N2B interactions) confirming its medium strength character.[84] The $S(D)\%$ is larger than $S(A)\%$ for all hydrogen bonds present in the **9aa*H$_2$O**. For **9aa*HCl** this condition was fulfilled for the interactions between water and chloride ion (Table 5). The last two criteria are rather characteristic for the isolated hydrogen bonds. In general, these interactions can be classified as isolated hydrogen bonds with some features of polarization-assisted hydrogen bonds supported by electrostatic forces. However, the polarization assistance is larger for **9aa*HCl**, especially for the N1–H13⋯Cl1, N1–H12⋯Cl1 and N1–H14⋯O1 hydrogen bonds, where $S\%(D)$ is smaller than $S\%(A)$ contribution.

3.5. Intermolecular interactions in macromolecular systems

Since some acridines and their derivatives display biological activities and interact with certain macromolecules such as double-stranded DNA[86] or proteins,[87] we decided to include a short analysis of the **9aa** interatomic interactions in existing macromolecular complexes to check if any significant changes could occur upon protonation. Due to lower resolution and accuracy of available X-ray structures of proteins, a reasonable

approach to study intermolecular interactions with **9aa** in a quantitative manner is to use Hirshfeld surfaces. We selected two entries from PDB database, namely 3tzb (quinone oxidoreductase)[88] and 6o4x (human acetylcholinesterase)[89] for further studies (Fig. S8 and Table S5†). Similarly, to previously discussed crystal structures, one of the leading features is the presence of sharp spikes in the bottom parts of 2D fingerprint plots, which are associated with the appearance of strong and medium O⋯H and C–H⋯O hydrogen bonds. Various π-stacking interactions also are present including T-shaped and sandwich-forms as well as cationic stacking. The two main changes in intermolecular interactions were observed. (i) Protonated **9aa** in acetylcholinesterase lead to formation of the additional H-bond between N10 and the carbonyl group in the peptide bond of a histidine residue. (ii) Protonation of **9aa**
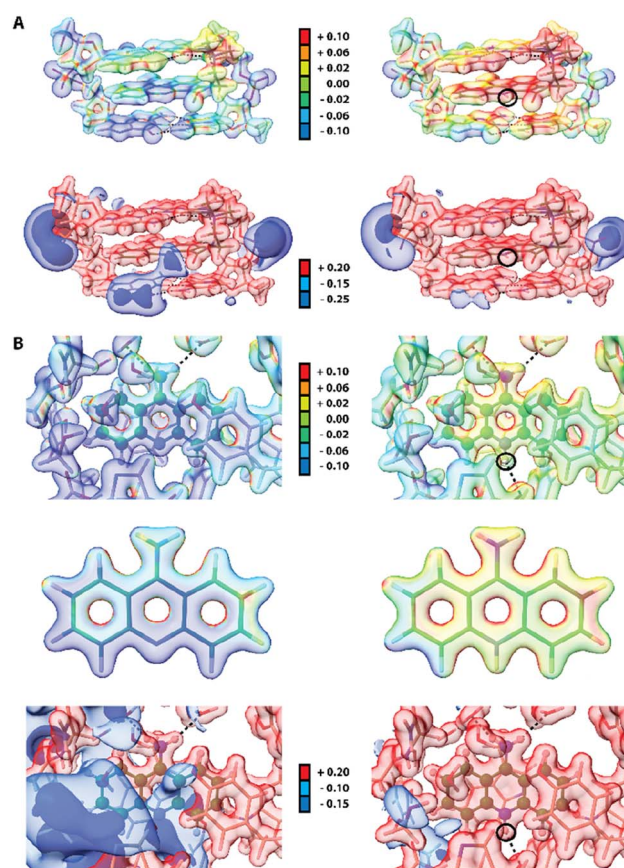

Fig. 8 Effect of protonation on electrostatic properties of macromolecular complexes of **9aa** and 9AD. In each case the electrostatic potential (ESP) is mapped on isosurfaces of electron density (contour 0.08 e Å^{-3}) prepared using a rainbow gradient colouring scheme where the lowest ESP values are blue and the highest are red (-0.1 to $+0.1$ E_h e^{-1}). Isosurfaces of electrostatic potential at several selected values are also presented. H-bonds are depicted as black dotted lines and black circles indicate a ligand protonation site. (A) Complex of DNA and 9AD in its neutral (left) and protonated (right) form. ESP mapped onto electron density (top) and isosurfaces of ESP (bottom). (B) **9aa** bound to human acetylcholinesterase in its neutral (left) and protonated (right) form (top). ESP mapped onto electron density for the ligand binding site (top) and **9aa** extracted from the complex. (Middle) Isosurfaces of ESP are presented at the bottom. **9aa** is depicted in ball and stick representation.

changes the character of stacking interactions between the NH_2/NH_3^+ group of **9aa** and a Trp residue, from T-shaped (neutral) to cationic (charged) in the quinone oxidoreductase.

Since electrostatic potential (ESP) often plays a vital role in molecular recognition in biological systems[90,91] we also compute ESP for two macromolecular complexes: previously mentioned human acetylcholinesterase and DNA complexed by 9-amino-*N*-(2-dimethylaminoethyl)acridine-4-carboxamide (9AD, PDB entry 465d).[92] The results indicate significant change in electrostatic potential upon protonation of the ligands (Fig. 8). Since 9AD intercalates between DNA pairs changes in protonation state of its aromatic system led to a visible impact on the charge distribution in the DNA molecule, while the electron density itself is virtually unchanged except for the very close proximity of the protonation site. In physiological condition 9AD exists almost exclusively in the protonated form, which has a stronger affinity to the negatively charged DNA than the neutral form. A similar situation occurs in acetylcholinesterase where protonation of **9aa** modifies the charge distribution in the entire binding site. Contrastingly, due to presence of large and negatively charged chlorine anions in the crystal structure of protonated **9aa**, the changes in ESP are much less noticeable upon protonation of **9aa** in the crystal state (Fig. S9†). For both complexes protonation does not have a significant effect on ED Laplacian and Electron Localization Function (ELF) beyond the ligand molecule itself. However aromatic residues near the **9aa** molecule are affected by protonation to some extend which is reflected in Laplacian changes in the aromatic residues in the ligand vicinity.

4. Conclusions

We have analysed the influence of the protonation of the 9-aminoacridine moiety in terms of quantitative and qualitative investigations of intermolecular interactions present in the studied crystal structures as well as topological properties obtained from the theoretical electron densities.

Our investigation was focused on the regions of the N-atom and amine group of 9-aminoacridine. Detailed examination of the electron density distribution and bond lengths due to protonation showed that protonation barely changes the electron distribution around protonated N-atoms. Also, no significant changes in the corresponding bond lengths were observed.

However, the ED distribution in the proximity of the amine group and water molecule is changed, and a decrease of the ED at BCP for N/O–H bonds is visible, which is related to the presence of the chloride anion. In contrast, our examination of the atomic charges showed that protonation influences only the atomic charge of the protonated N2 atom. Investigation of the electron density at BCP for hydrogen bonds revealed their medium-strength character, however, we have obtained an unconventional set of source function contributions from the donor, acceptor, and the hydrogen atoms. Based on this analysis, we can conclude that investigated hydrogen bonds are isolated, with some polarization features and contribution of electrostatic forces, which increases its polarization effect for the protonated form.

Protonation changes the molecular architecture of the crystal structures, and thus modifies the intermolecular interactions. The analysis of the Hirshfeld surface and 2D fingerprints plots revealed that the different orientation of the acridine moiety after protonation has a significant effect on the proportion of N⋯H and O⋯H contacts. Namely, **9aa** participates in fewer N⋯H contacts after protonation. On the contrary, the contribution of the O⋯H contacts almost doubled upon protonation. In addition, protonation also changed the number of weak interactions: the number of C⋯H interactions decreased while the number of H⋯H interactions increased.

Theoretical calculations of energetic features for dimers and crystal lattice proved the differences between neutral and protonated forms of this compound. Protonation stabilizes crystal structure due to the presence of strong hydrogen bonds, which compensate destabilizing effect associated with the interactions between two 9-aminoacridine cations. In general, in the case of studied systems, electrostatic forces have a dominant role in the stabilization of crystal lattice. Additionally, crystal structure after protonation displays less molecular crowding, decreasing the repulsive forces.

The results of our work agree with the previously reported differences observed between the neutral and protonated forms for certain APIs.[23,24,87] Each form of **9aa** should have different solubility in physiological conditions. Due to the presence of strong repulsive forces in the crystal lattice of protonated **9aa**, it should have greater solubility in polar solvents and be more likely to host more water molecules. Quantum crystallography can be successfully used in investigation of charge distribution and may lead to improvement in drug design and help in the prediction of crystal structure properties.

Author contributions

SP: crystallization of **9aa** neutral, XRD experiment for **9aa** neutral, data reduction for the **9aa** neutral, HARs for **9aa** neutral and protonated, QTAIM/SF analyses for all refinements, calculations in CE, Crystal09 and Crystal17, conceptualization and writing original draft, preparation of all tables and figures presented in publication and ESI.† MZ: writing of the introduction, text reviewing, macromolecular studies AM: XRD experiment for **9aa** protonated, data reduction for **9aa** protonated DT: crystallization of **9aa** neutral, assistance in XRD experiments, conceptualization KW: funding, supervising, editing, correcting of the text, discussion of results.

Conflicts of interest

There are no conflicts of interest to declare.

Acknowledgements

References

1 M. E. Rodriguez, K. Azizuddin, P. Zhang, S. Chiu, M. Lam, M. E. Kenney, C. Burda and N. L. Oleinick, *Mitochondrion*, 2008, **8**, 237–246.

2 M. Gensicka-Kowalewska, G. Cholewiński and K. Dzierzbicka, *RSC Adv.*, 2017, **7**, 15776–15804.

3 A. Schmidt and M. Liu, in *Advances in Heterocyclic Chemistry*, Elsevier, 2015, vol. 115, pp. 287–353.

4 Q.-B. Zhang, Y.-L. Ban, D.-G. Zhou, P.-P. Zhou, L.-Z. Wu and Q. Liu, *Org. Lett.*, 2016, **18**, 5256–5259.

5 N. J. Pritchard, A. Blake and A. R. Peacocke, *Nature*, 1966, **212**, 1360–1361.

6 J. M. Crenshaw, D. E. Graves and W. A. Denny, *Biochemistry*, 1995, **34**, 13682–13687.

7 J. V. Walker and J. L. Nitiss, *Cancer Invest.*, 2002, **20**, 570–589.

8 M. Fonte, N. Tassi, P. Gomes and C. Teixeira, *Molecules*, 2021, **26**, 600.

9 P. Varakumar, K. Rajagopal, B. Aparna, K. Raman, G. Byran, C. M. Gonçalves Lima, S. Rashid, M. H. Nafady, T. B. Emran and S. Wybraniec, *Molecules*, 2022, **28**, 193.

10 C. Guo, A. V. Gasparian, Z. Zhuang, D. A. Bosykh, A. A. Komar, A. V. Gudkov and K. V. Gurova, *Oncogene*, 2009, **28**, 1151–1161.

11 Y.-W. Sun, K.-Y. Chen, C.-H. Kwon and K.-M. Chen, *Mol. Med. Rep.*, 2016, **13**, 933–938.

12 S. Kumar, M. Guha, V. Choubey, P. Maity and U. Bandyopadhyay, *Life Sci.*, 2007, **80**, 813–828.

13 C. Teixeira, N. Vale, B. Pérez, A. Gomes, J. R. B. Gomes and P. Gomes, *Chem. Rev.*, 2014, **114**, 11164–11220.

14 E. Schur, J. Bernstein, L. S. Price, R. Guo, S. L. Price, S. H. Lapidus and P. W. Stephens, *Cryst. Growth Des.*, 2019, **19**, 4884–4893.

15 A. Kupka, V. Vasylyeva, D. W. M. Hofmann, K. V. Yusenko and K. Merz, *Cryst. Growth Des.*, 2012, **12**, 5966–5971.

16 X. Mei and C. Wolf, *Cryst. Growth Des.*, 2004, **4**, 1099–1103.

17 A. Sikorski and D. Trzybiński, *Tetrahedron*, 2011, **67**, 1479–1484.

18 A. Sikorski and D. Trzybiński, *Tetrahedron Lett.*, 2013, **54**, 1463–1466.

19 A. Sikorski and D. Trzybiński, *J. Mol. Struct.*, 2013, **1049**, 90–98.

20 D. Trzybiński and A. Sikorski, *CrystEngComm*, 2013, **15**, 6808.

21 M. Pourayoubi, H. Eshtiagh-Hosseini, S. Sanaei Ataabadi, T. Mancilla Percino and M. A. Leyva Ramírez, *Acta Crystallogr., Sect. E: Struct. Rep. Online*, 2011, **67**, o565.

22 L. Gaohua, X. Miao and L. Dou, *Expert Opin. Drug Metab. Toxicol.*, 2021, **17**, 1103–1124.

23 N. J. Yang and M. J. Hinner, in *Site-Specific Protein Labeling*, ed. A. Gautier and M. J. Hinner, Springer, New York, NY, 2015, vol. 1266, pp. 29–53.

24 A. Mitra, F. Kesisoglou, M. Beauchamp, W. Zhu, F. Chiti and Y. Wu, *Mol. Pharm.*, 2011, **8**, 2216–2223.

25 A. Mitra and F. Kesisoglou, *Mol. Pharm.*, 2013, **10**, 3970–3979.

26 T. L. Russell, R. R. Berardi, J. L. Barnett, T. L. O'Sullivan, J. G. Wagner and J. B. Dressman, *Pharm. Res.*, 1994, **11**, 136–143.

27 P. A. Dickinson, R. Abu Rmaileh, L. Ashworth, R. A. Barker, W. M. Burke, C. M. Patterson, N. Stainforth and M. Yasin, *AAPS J.*, 2012, **14**, 196–205.

28 S. Grabowsky, A. Genoni and H.-B. Bürgi, *Chem. Sci.*, 2017, **8**, 4159–4176.

29 L. Bučinský, D. Jayatilaka and S. Grabowsky, *J. Phys. Chem. A*, 2016, **120**, 6650–6669.

30 S. Pawlędzio, M. Malinska, M. Woińska, J. Wojciechowski, L. Andrade Malaspina, F. Kleemiss, S. Grabowsky and K. Woźniak, *IUCrJ*, 2021, **8**, 608–620.

31 S. Pawlędzio, M. Malinska, F. Kleemiss, S. Grabowsky and K. Woźniak, *Inorg. Chem.*, 2022, **61**, 4235–4239.

32 M. Kulik and P. M. Dominiak, *Comput. Struct. Biotechnol. J.*, 2022, **20**, 6237–6243.

33 A. Genoni, L. Bučinský, N. Claiser, J. Contreras-García, B. Dittrich, P. M. Dominiak, E. Espinosa, C. Gatti, P. Giannozzi, J. Gillet, D. Jayatilaka, P. Macchi, A. Ø. Madsen, L. Massa, C. F. Matta, K. M. Merz, P. N. H. Nakashima, H. Ott, U. Ryde, K. Schwarz, M. Sierka and S. Grabowsky, *Chem.–Eur. J.*, 2018, **24**, 10881–10905.

34 D. Jayatilaka and B. Dittrich, *Acta Crystallogr., Sect. A: Found. Crystallogr.*, 2008, **64**, 383–393.

35 S. C. Capelli, H.-B. Bürgi, B. Dittrich, S. Grabowsky and D. Jayatilaka, *IUCrJ*, 2014, **1**, 361–379.

36 M. L. Davidson, S. Grabowsky and D. Jayatilaka, *Acta Crystallogr., Sect. B: Struct. Sci., Cryst. Eng. Mater.*, 2022, **78**, 312–332.

37 S. Pawlędzio, M. Malinska, F. Kleemiss, S. Grabowsky and K. Woźniak, *IUCrJ*, 2022, **9**, 497–507.

38 M. Woińska, S. Grabowsky, P. M. Dominiak, K. Woźniak and D. Jayatilaka, *Sci. Adv.*, 2016, **2**, e1600192.

39 L. A. Malaspina, A. Genoni, D. Jayatilaka, M. J. Turner, K. Sugimoto, E. Nishibori and S. Grabowsky, *J. Appl. Crystallogr.*, 2021, **54**, 718–729.

40 M. Wanat, M. Malinska, M. J. Gutmann, R. I. Cooper and K. Wozniak, *Acta Crystallogr., Sect. B: Struct. Sci., Cryst. Eng. Mater.*, 2021, **77**, 41–53.

41 M. Ziemniak, S. Pawlędzio, A. Zawadzka-Kaźmierczuk, P. M. Dominiak, D. Trzybiński, W. Koźmiński, R. Zieliński, I. Fokt, W. Priebe, K. Woźniak and B. Pająk, *RSC Adv.*, 2022, **12**, 8345–8360.

42 N. Heidari, A. Tarahhomi and A. van der Lee, *ChemistrySelect*, 2022, **7**(29), e202201504.

43 F. Kleemiss, E. K. Wieduwilt, E. Hupf, M. W. Shi, S. G. Stewart, D. Jayatilaka, M. J. Turner, K. Sugimoto, E. Nishibori, T. Schirmeister, T. C. Schmidt, B. Engels and S. Grabowsky, *Chem.–Eur. J.*, 2021, **27**, 3407–3419.

44 L. K. Saunders, A. R. Pallipurath, M. J. Gutmann, H. Nowell, N. Zhang and D. R. Allan, *CrystEngComm*, 2021, **23**, 6180–6190.

45 Bruker, *APEX2*, Bruker AXS Inc., Madison, Wisconsin, USA, 2012.

46 M. J. Buerger and G. E. Klein, *J. Appl. Phys.*, 1945, **16**, 408–418.

47 R. H. Blessing, *Acta Crystallogr., Sect. A: Found. Crystallogr.*, 1995, **51**, 33–38.

48 G. M. Sheldrick, *Acta Crystallogr., Sect. A: Found. Crystallogr.*, 1990, **46**, 467–473.

49 G. M. Sheldrick, *Acta Crystallogr., Sect. A: Found. Crystallogr.*, 2008, **64**, 112–122.

50 G. M. Sheldrick, *Acta Crystallogr., Sect. C: Struct. Chem.*, 2015, **71**, 3–8.

51 O. V. Dolomanov, L. J. Bourhis, R. J. Gildea, J. a. K. Howard and H. Puschmann, *J. Appl. Crystallogr.*, 2009, **42**, 339–341.

52 M. L. Chodkiewicz, S. Migacz, W. Rudnicki, A. Makal, J. A. Kalinowski, N. W. Moriarty, R. W. Grosse-Kunstleve, P. V. Afonine, P. D. Adams and P. M. Dominiak, *J. Appl. Crystallogr.*, 2018, **51**, 193–199.

53 L. J. Bourhis, O. V. Dolomanov, R. J. Gildea, J. A. K. Howard and H. Puschmann, *Acta Crystallogr., Sect. A: Found. Adv.*, 2015, **71**, 59–75.

54 F. Neese, *Wiley Interdiscip. Rev.: Comput. Mol. Sci.*, 2012, **2**, 73–78.

55 F. Neese, F. Wennmohs, U. Becker and C. Riplinger, *J. Chem. Phys.*, 2020, **152**, 224108.

56 D. S. Sholl and J. A. Steckel, *Density Functional Theory: A Practical Introduction*, John Wiley & So, Ltd, 2009.

57 T. H. Dunning, *J. Chem. Phys.*, 1989, **90**, 1007–1023.

58 C. Gatti, V. R. Saunders and C. Roetti, *J. Chem. Phys.*, 1994, **101**, 10686–10696.

59 M. Ernst, A. Genoni and P. Macchi, *J. Mol. Struct.*, 2020, 127975.

60 A. Ø. Madsen, *J. Appl. Crystallogr.*, 2006, **39**, 757–758.

61 R. F. W. Bader, *Atoms in Molecules: A Quantum Theory*, Oxford University Press, Oxford, New York, 1994.

62 T. A. Keith, *AIMAll (Version 19.10.12) TK Gristmill Software*, Overland Park KS, USA, 2019, https://aim.tkgristmill.com.

63 R. Dovesi, R. Orlando, B. Civalleri, C. Roetti, V. R. Saunders and C. M. Zicovich-Wilson, *Z. Kristallogr. - Cryst. Mater.*, 2009, **220**, 571–573.

64 R. Dovesi, A. Erba, R. Orlando, C. M. Zicovich-Wilson, B. Civalleri, L. Maschio, M. Rérat, S. Casassa, J. Baima, S. Salustro and B. Kirtman, *Wiley Interdiscip. Rev.: Comput. Mol. Sci.*, 2018, **8**, e1360.

65 D. Vilela Oliveira, J. Laun, M. F. Peintinger and T. Bredow, *J. Comput. Chem.*, 2019, **40**, 2364–2376.

66 S. Grimme, *J. Comput. Chem.*, 2004, **25**, 1463–1473.

67 S. Grimme, J. Antony, S. Ehrlich and H. Krieg, *J. Chem. Phys.*, 2010, **132**, 154104.

68 S. F. Boys and F. Bernardi, *Mol. Phys.*, 1970, **19**, 553–566.

69 C. F. Mackenzie, P. R. Spackman, D. Jayatilaka and M. A. Spackman, *IUCrJ*, 2017, **4**, 575–587.

70 J. Zhang and T. Lu, *Phys. Chem. Chem. Phys.*, 2021, **23**, 20323–20328.

71 T. Lu and F. Chen, *J. Comput. Chem.*, 2012, **33**, 580–592.

72 E. C. Meng, T. D. Goddard, E. F. Pettersen, G. S. Couch, Z. J. Pearson, J. H. Morris and T. E. Ferrin, *Protein Sci.*, 2023, **32**, e4792.

73 A. J. Schaefer, V. M. Ingman and S. E. Wheeler, *J. Comput. Chem.*, 2021, **42**, 1750–1754.

74 J.-D. Chai and M. Head-Gordon, *Phys. Chem. Chem. Phys.*, 2008, **10**, 6615–6620.

75 F. Weigend and R. Ahlrichs, *Phys. Chem. Chem. Phys.*, 2005, **7**, 3297–3305.

76 A. V. Marenich, C. J. Cramer and D. G. Truhlar, *J. Phys. Chem. B*, 2009, **113**, 6378–6396.

77 S. Chaudhuri, *J. Chem. Soc. Chem. Commun.*, 1983, 1242–1243.

78 R. Talacki, H. L. Carrell, J. P. Glusker and IUCr, *Acta Crystallogr., Sect. B: Struct. Crystallogr. Cryst. Chem.*, 1974, **30**, 1044–1047.

79 A. H. Compton, *Nature*, 1915, **95**, 343–344.

80 D. Tchoń, A. Makal, M. Gutmann and K. Woźniak, *Z. Kristallogr. - Cryst. Mater.*, 2018, **233**, 649–661.

81 C. Gatti, F. Cargnoni and L. Bertini, *J. Comput. Chem.*, 2003, **24**, 422–436.

82 L. J. Farrugia, C. Evans and M. Tegel, *J. Phys. Chem. A*, 2006, **110**, 7952–7961.

83 L. J. Farrugia, C. Evans, D. Lentz and M. Roemer, *J. Am. Chem. Soc.*, 2009, **131**, 1251–1268.

84 I. Rozas, I. Alkorta and J. Elguero, *J. Am. Chem. Soc.*, 2000, **122**, 11154–11161.

85 A. Krawczuk and P. Macchi, *Chem. Cent. J.*, 2014, **8**, 68.

86 S. Neidle and M. Sanderson, in *Principles of Nucleic Acid Structure*, ed. S. Neidle and M. Sanderson, Academic Press, New York, 2nd edn, 2022, pp. 191–286.

87 P. Mitra, U. Pal, N. C. Maiti, A. Ghosh, A. Bhunia and S. Basu, *RSC Adv.*, 2016, **6**, 53454–53468.

88 K. A. Nolan, M. S. Dunstan, M. C. Caraher, K. A. Scott, D. Leys and I. J. Stratford, *Mol. Cancer Ther.*, 2012, **11**, 194–203.

89 O. Gerlits, K.-Y. Ho, X. Cheng, D. Blumenthal, P. Taylor, A. Kovalevsky and Z. Radić, *Chem.-Biol. Interact.*, 2019, **309**, 108698.

90 F. Vascon, M. Gasparotto, M. Giacomello, L. Cendron, E. Bergantino, F. Filippini and I. Righetto, *Comput. Struct. Biotechnol. J.*, 2020, **18**, 1774–1789.

91 G. Grassmann, L. Di Rienzo, G. Gosti, M. Leonetti, G. Ruocco, M. Miotto and E. Milanetti, *Sci. Rep.*, 2023, **13**, 10207.

92 A. Adams, J. M. Guss, C. A. Collyer, W. A. Denny and L. P. G. Wakelin, *Biochemistry*, 1999, **38**, 9221–9233.